

This is the **accepted version** of the article:

de Rojas, Julius; Quintana, Alberto; Lopeandía Fernández, Aitor; [et al.]. «Boosting room-temperature magneto-ionics in a non-magnetic oxide semiconductor». Advanced Functional Materials, Vol. 30, Issue 36 (September 2020), art. 2003704. DOI 10.1002/adfm.202003704

This version is available at <https://ddd.uab.cat/record/233360>

under the terms of the  ^{IN}
COPYRIGHT license

Boosting room-temperature magneto-ionics in a non-magnetic oxide semiconductor

Julius de Rojas, Alberto Quintana, Aitor Lopeandía, Joaquín Salguero, José L. Costa-Krämer, Llibertat Abad, Maciej O. Liedke, Maik Butterling, Andreas Wagner, Lowie Henderick, Jolien Dendooven, Christophe Detavernier, Jordi Sort, Enric Menéndez**

Dr. Julius de Rojas, Dr. A. Lopeandía, Prof. J. Sort, Dr. E. Menéndez

Departament de Física, Universitat Autònoma de Barcelona, E-08193 Cerdanyola del Vallès, Spain

E-mail: jordi.sort@uab.cat; enric.menendez@uab.cat

Dr. A. Quintana

Department of Physics, Georgetown University, Washington, D.C. 20057, United States

J. Salguero, Dr. J. L. Costa-Krämer

IMN-Instituto de Micro y Nanotecnología (CNM-CSIC), Isaac Newton 8, PTM, 28760 Tres Cantos, Madrid, Spain

Dr. Ll. Abad

Institut de Microelectrònica de Barcelona, IMB-CNM (CSIC), Campus UAB, E-08193 Bellaterra, Spain

Dr. M. O. Liedke, Dr. M. Butterling, Dr. A. Wagner

Institute of Radiation Physics, Helmholtz-Center Dresden-Rossendorf, Dresden 01328, Germany

L. Henderick, Prof. J. Dendooven, Prof. C. Detavernier

Department of Solid State Sciences, CoCooN, Ghent University, Krijgslaan 281/S1, 9000 Ghent, Belgium

Prof. J. Sort

Institució Catalana de Recerca i Estudis Avançats (ICREA), Pg. Lluís Companys 23, E-08010 Barcelona, Spain

Keywords: magnetoelectric effects, magneto-ionics, transistor, capacitor, low-power spintronics

Voltage control of magnetism through electric field-induced oxygen motion (magneto-ionics) could represent a significant breakthrough in the pursuit for new strategies to enhance energy efficiency in magnetically-actuated devices. Boosting the induced changes in magnetization, magneto-ionic rates and cyclability continue to be key challenges to turn magneto-ionics into real applications. Here it is demonstrated that room-temperature magneto-ionic effects in electrolyte-gated paramagnetic Co_3O_4 films can be largely increased both in terms of generated magnetization (6 times larger) and speed (35 times faster) if the electric field is applied using an electrochemical capacitor configuration (utilizing an underlying conducting buffer layer) instead of placing the electric contacts at the side of the semiconductor (electric-double-layer transistor-like configuration). This is due to a greater uniformity and strength of the electric field in the capacitor design. These results are appealing to widen the use of ion migration in technological applications such as neuromorphic computing or iontronics in general.

1. Introduction

Current computers rely on Von Neumann's structural design in which the central processing unit and memory constitute different sub-devices bridged by the communication bus. This is not only detrimental to data processing speed but also to energy efficiency, making the search for new computing architectures central for future information technologies.^[1–6] Neuromorphic computing relies on the use of devices that emulate the electrical behavior of the biological synapse, which is the memory and learning element of the brain, and has emerged as an alternative, which could render low-power information storage/processing.^[2–4,6] Intense research is currently being carried out in the use of electronic-^[2,3] and spintronic-based^[4,5] approaches to mimic synapse's activity. However, so far, these strategies are ultimately based on the use of electric currents (to generate magnetic fields through electromagnetic induction or spin-polarized electric currents via spin-transfer torque), involving a significant energy loss

by heat dissipation through Joule effect.^[7,8] The same problem of power consumption is, in fact, encountered in conventional magnetic storage systems (hard disks, magnetic random-access memories), where a large fraction of the incoming electric power (up to 40%) can be wasted in the form of heat dissipation.

Voltage control of magnetism (VCM), wherein magnetism is controlled via an applied electric field in place of an electric current, could potentially represent a significant breakthrough, envisaging ultra-low power emulation of the biological synapse.^[5] VCM has been also proposed as a suitable strategy to develop new types of high-density, low-power data storage devices, such as magneto-electric random-access memories.^[9] Besides its potential use in memories and computation, magnetoelectric materials have also shown potential, in recent years, to be used in magnetic micro-electro-mechanical systems, such as biomagnetic sensors,^[10] where effects induced at moderate rates (*e.g.*, 1 s) are appealing to boost energy efficiency.

VCM has conventionally branched into three broad approaches, including (i) single-phase, multiferroic materials,^[11] (ii) inverse magnetostriction effects in piezoelectric/ferromagnetic heterostructures,^[12,13] and (iii) surface charge accumulation in ferromagnetic metals (*i.e.*, direct electric field effect).^[14–20] Each of the aforementioned VCM mechanisms has some drawbacks: multiferroics are limited in number, particularly at room-temperature; strain-mediated heterostructures suffer from mechanical fatigue; and, in metals and alloys, electronic charging is only observed in ultra-thin^[14,15] or highly porous^[16–20] ferromagnetic films.

Electric field-induced oxygen motion in magnetic materials (magneto-ionics) has recently revolutionized VCM since this mechanism may allow for a voltage-driven modulation of magnetic properties, such as coercivity, exchange bias field or magnetic anisotropy, to a level never reached by any other magnetoelectric means (*i.e.*, approaches (i), (ii) and (iii) above).^[6,21–34] Magneto-ionics, with magnetoelectric coupling efficiencies of the order of 10^3 fJ/(V·m), might render energies per writing event as low as $\sim 10^{-3}$ fJ = 1 aJ.^[22,28] This represents energies two and five orders of magnitude lower than that required in complementary metal oxide

semiconductor (CMOS) technology ($\sim 10^{-1}$ fJ/bit) and magnetic-based devices like magneto-resistive random access memories or hard disk drives ($\sim 10^2$ fJ/bit), respectively.^[28]

Typically, magneto-ionic systems consist of layered heterostructures in which ferromagnetic metals, such as Co^[22] or Fe,^[28] are grown adjacent to GdO_x or HfO₂ layers, which act as ion reservoirs and, thereby, accepting or donating oxygen ions depending on the voltage polarity. Room-temperature ionic motion of oxygen is slow, involving times between $10^2 - 10^3$ s ($10^{-2} - 10^{-3}$ Hz in frequency rate) to switch the magnetic state, such as the magnetic anisotropy easy axis from out-of-plane to in-plane and *vice versa* in ultra-thin Co layers by voltage-driven oxygen migration from a GdO_x reservoir.^[22] By heterostructure miniaturization (from 55 nm down to 18 nm in thickness, *i.e.*, around 3 times reduction), times ~ 10 s have been achieved.^[22] Therefore, alongside the applied voltage, these solid electrolytes usually require of high temperatures since ion migration is a thermally activated process.^[22–24,29,30] In these magneto-ionic systems, the pristine ferromagnetic layer suffers from pronounced structural and compositional changes, leading to irreversibility^[23] and, thus, poor cyclability.^[22] Recently, via a proton-based approach, excellent endurance and 10^{-1} s (10 Hz) room-temperature operation has been shown feasible in spite of certain instability since hydrogen retention is limited.^[29] Moreover, voltage-induced changes of magnetization have also been achieved by the insertion/removal of ions other than oxygen, such as Li^[35,36] or F ions.^[37]

An alternative approach is the use of structural oxygen (self-contained in the magnetic material of interest), hence avoiding the need of external oxygen sources.^[26] This has been shown in electrolyte-gated paramagnetic Co₃O₄ films, in which room-temperature voltage-controlled on-off ferromagnetism has been achieved by electric switching of the oxidation state of cobalt (*i.e.*, voltage-driven reduction/oxidation), taking advantage of the defect-assisted voltage-driven migration of structural oxygen.^[26] Even though this route still yields slow room-temperature

magneto-ionic motion, it shows outstanding stability and promising cyclability since the target is already oxidized.

Herein, we demonstrate that, without degrading cyclability, room-temperature magneto-ionic motion in electrolyte-gated, paramagnetic and fairly thick Co_3O_4 films (thicknesses above 100 nm) can be enhanced in terms of both generated magnetization (6 times larger) and speed (35 times faster) by using an electrochemical capacitor configuration (*i.e.*, with a suitable conducting buffer layer grown underneath the oxide film) rather than just making the contacts on top or at the sides of the semiconducting layer (configuration analogous to an electric-double-layer transistor,^[38,39] without an underlying metallic seed layer), as in some previous works from the literature.^[26,40–43] The presence of this underlying conducting metallic layer in the capacitor configuration largely enhances the uniformity and strength of the electric field generated across the oxide film when voltage is applied. Our results, showing the importance of properly optimizing device design to apply electric field, could extend the use of oxygen magneto-ionics in new types of MEMS devices, energy storage systems (batteries), iontronics^[43] and, specifically, in brain-inspired computing,^[39] which demand endurance and moderate speed of operation.^[44]

2. Results

Figure 1a and **1b** show the two types of film structures (Co_3O_4 (130 nm)/ SiO_2 (20 nm)/(100)-oriented Si substrate –transistor-like configuration– and Co_3O_4 (130 nm)/TiN (170 nm)/(100)-oriented Si substrate –capacitor configuration–) investigated in this work, aimed at unraveling the role of the design of electric field actuation to apply electric field in the magneto-ionic response of Co_3O_4 . In contrast to SiO_2 , the TiN buffer layer is conducting.^[45]

Electrolyte-gating is used to generate the electric field while performing in-plane vibrating sample magnetometry (VSM) –*i.e.*, magnetoelectric measurements–. A Pt wire is used as counter electrode/gate electrode (see Experimental Section for further details). The as-prepared

Co₃O₄ sample in the transistor-like configuration shows residual ferromagnetic behavior ($< 2 \text{ emu/cm}^{-3}$), whereas the as-prepared Co₃O₄ film in the electrochemical capacitor configuration exhibits some traces of ferromagnetic signal $< 10 \text{ emu/cm}^{-3}$ (Figure 1c, 1d and 1e, and Figure S1). This mild ferromagnetism could be ascribed to local deviations of Co₃O₄ stoichiometry, in particular at the TiN-Co₃O₄ interface since the deposition of Co₃O₄ is carried out at 200 °C and the thermal stability of TiN is lower than that of SiO₂. Anyhow, the films are ruled by an overall paramagnetic behavior at room-temperature.^[26]

To investigate magneto-ionics in each configuration, the samples were subjected to -50 V for several hours and magnetic hysteresis loops of 25 min of duration were continuously recorded. After subjecting each sample to -50 V for 25 min (*i.e.*, upon the first hysteresis loop is recorded), the measurements show a clear hysteretic behavior, evidencing the emergence of ferromagnetism. The capacitor configuration shows a remarkable increase in magnetization upon sweeping the first quadrant of the first hysteresis cycle, which doubles once the measurement reaches the fourth quadrant of the first loop. A much more gradual increase of the magnetization is observed in the transistor-like configuration (see Figure S2 to observe the evolution of the magnetization with time for the first hysteresis loop of both configurations). Figure 1e shows the saturation magnetization (M_S) as a function of time (see Figure S3 for information on M_S quantification). The magnetic moment scales monotonically with time for each configuration, but with a 6-fold larger increase between the transistor-like and capacitor configurations in the total magnetization (118.5 to $699.2 \text{ emu cm}^{-3}$, respectively) reached after magneto-ionic motion has stabilized. Furthermore, the time scale for ferromagnetism generation (“on” state) in the capacitor configuration is significantly faster than in the transistor-like structure. To compare properly the rate of “on” switching, this magnetization increase is determined by a linear fit of the M_S vs. t plot evaluated during the first minutes of voltage application (wherein M_S in the capacitor configuration fully saturates). The rates are 33.1 and

1170.8 emu cm⁻³ h⁻¹, showing that the use of a conducting buffer (capacitor) layer enhances ion migration by a factor 35 with respect to the insulating buffer layer (transistor-like).

Looking at the M (magnetization)- H (applied magnetic field) loops (Figure 1c and 1d), there are also marked shape differences. The capacitor configuration exhibits more square-shaped cycles (*i.e.*, it has a more “easy axis” character) than the transistor-like configuration. To examine the shape of the M - H loops, the squareness, defined as the ratio between the remnant magnetization (M_R) and M_S (M_R/M_S), and the slope of the hysteresis loop at the coercive field (H_C) normalized to M_S (dM/dH ($H = H_C$) M_S^{-1}) have been calculated for both the descending and ascending branches of the measured hysteresis loops (Figure 1f). The capacitor configuration exhibits higher M_R/M_S ratios and slopes at H_C (narrower distribution of coercive fields) throughout the time the voltage was applied, in concordance with more square-shaped.^[46]

To further examine the nature of the electric field experienced by the Co₃O₄ samples, COMSOL simulations were performed to model the initial voltage distributions for each configuration upon electrolyte-gating (see Experimental Section for further simulation details). In Figure 1g and 1h, electric contact to the working electrodes (Co₃O₄ and TiN for the transistor-like and capacitor configurations, respectively) is made at the top of the left plane which represents the samples, whereas the right plane corresponds to the counter electrode (*i.e.*, Pt wire).

Clear differences can be seen in the equipotential lines for the transistor-like (Figure 1g) and capacitor (Figure 1h) configurations. In the transistor-like structure, the dielectric nature of SiO₂ and limited electric conductivity of Co₃O₄^[47] manifest in a macroscopic, non-homogeneous voltage distribution along the vertical extent of the Co₃O₄ film, showing a weaker and less uniform applied electric field as the distance from the electric contact is increased. Conversely, in the capacitor configuration, the conducting nature of TiN results in a nearly uniform voltage distribution along the vertical cross-section of the sample, which gives rise to a larger and better-defined electric field along the direction perpendicular to the Co₃O₄ film plane. In

contrast to the transistor-like configuration, the whole Co_3O_4 film is straightaway activated here for magneto-ionic motion (Figure S4).

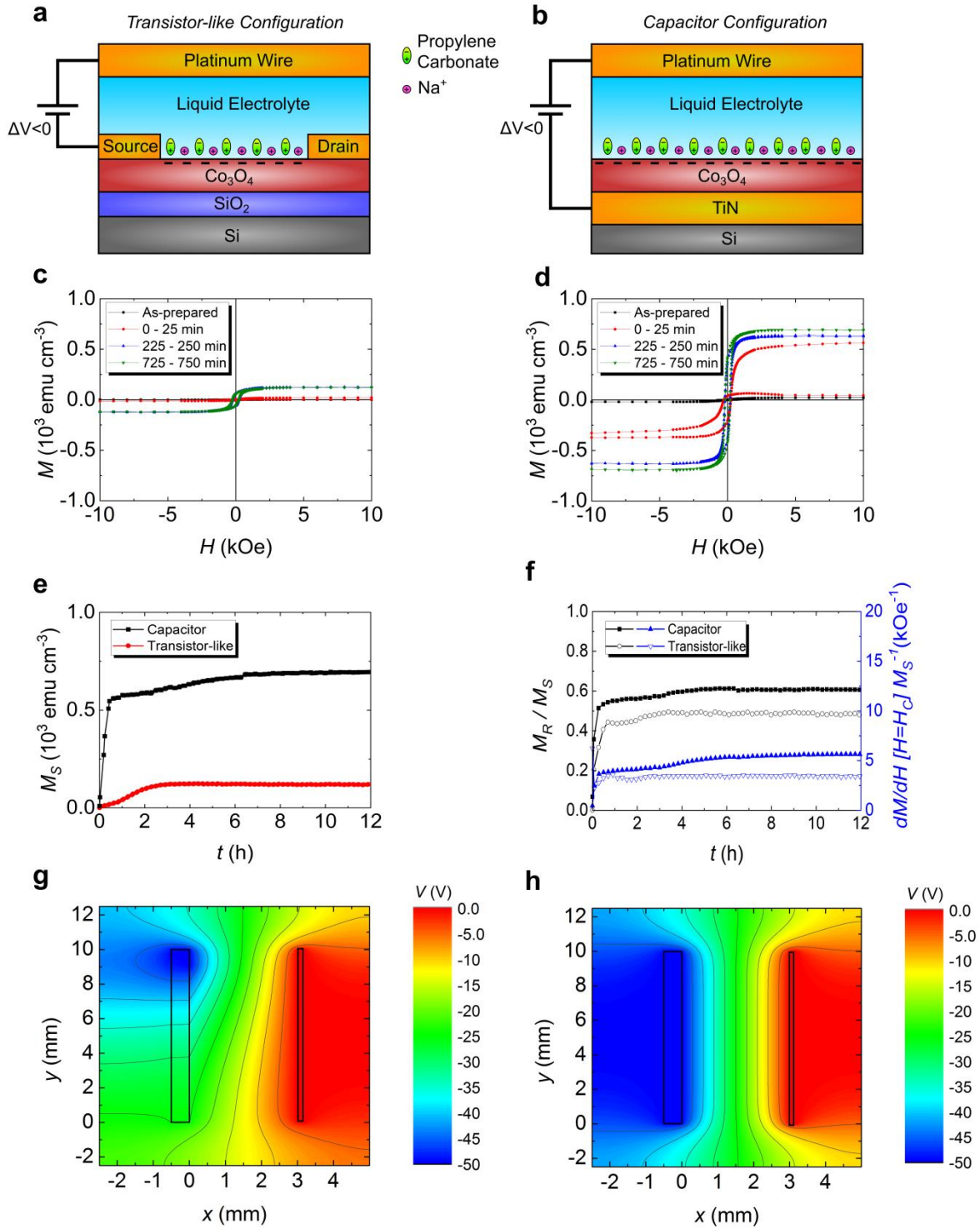


Figure 1. Sample configurations: a) Co_3O_4 on SiO_2 (electric-double-layer transistor-like configuration) and b) Co_3O_4 on TiN (capacitor configuration). c) and d) consecutive hysteresis loops under -50 V gating for the transistor-like and capacitor configurations, respectively, taken by in-plane vibrating sample magnetometry. e) Time evolution of the saturation magnetization (M_S vs. t) and f) squareness (M_R/M_S) & slope of hysteresis loop at H_C normalized to M_S for each configuration. g) and h) show the COMSOL

simulations of the initial voltage distribution at the moment in which the transistor-like and the capacitor configurations, respectively, are electrolyte-gated (equipotential lines are drawn).

To assess the degree of structural and compositional change that Co_3O_4 undergoes with voltage for the two investigated configurations, cross-section lamellae of the pristine and treated Co_3O_4 films were prepared and characterized by high-angle annular dark-field scanning transmission electron microscopy (HAADF-STEM) and electron energy loss spectroscopy (EELS), respectively (**Figure 2**).

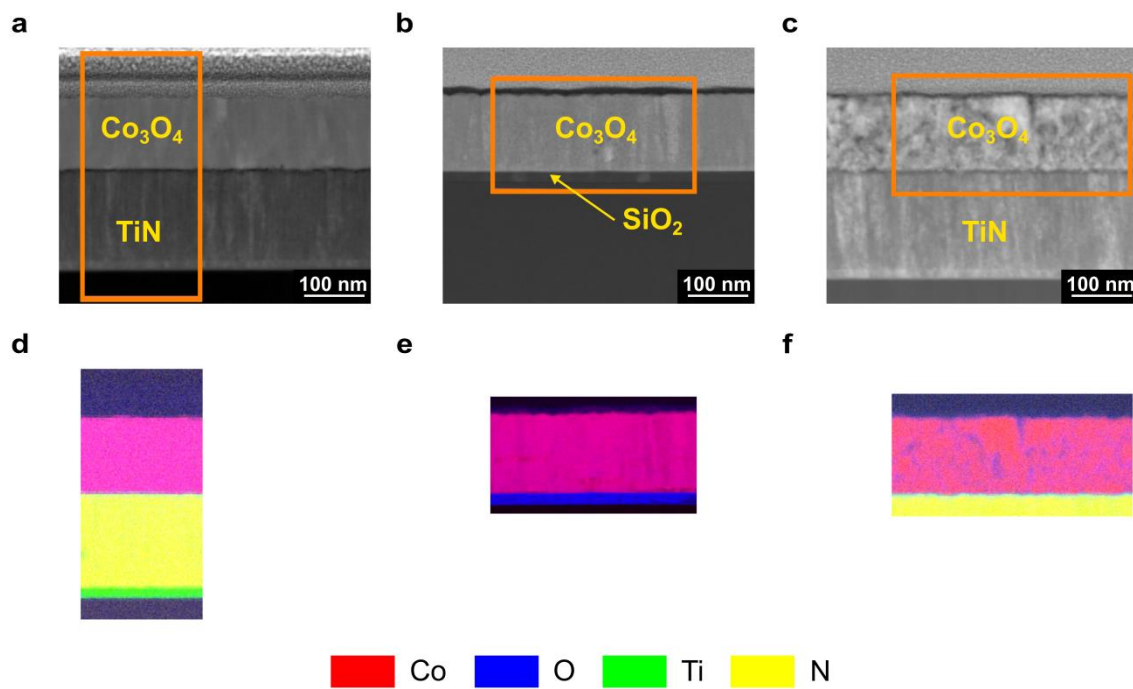


Figure 2. Structural and compositional characterization by high-angle annular dark-field scanning transmission electron microscopy (HAADF-STEM) and electron energy loss spectroscopy (EELS), respectively. a), b) and c) are HAADF-STEM images and d), e) and f) are in that order the corresponding elemental EELS mappings of the areas marked in orange of pristine $\text{Co}_3\text{O}_4/\text{TiN}$, $\text{Co}_3\text{O}_4/\text{SiO}_2$ negatively biased at -50 V for 80 min and $\text{Co}_3\text{O}_4/\text{TiN}$ also negatively biased at -50 V for 80 min, respectively. Colors corresponding to each element for the EELS analyses are depicted at the bottom of the figure.

The morphology of the pristine sample grown on TiN (Figure 2a) shows regular, columnar-shaped grains as it happens in Co_3O_4 deposited by atomic layer deposition on SiO_2 .^[26] This morphology remains rather unaltered after treating the Co_3O_4 film deposited on SiO_2 with -50 V for 80 min (Figure 2e). On the contrary, the Co_3O_4 morphology in the capacitor configuration

treated at -50 V for 80 min shows no columnar grains consistent with a more nanostructured Co_3O_4 phase (Figure 2c and Figure S5).

To locally quantify the Co/O distribution, Co and O EELS mappings were conducted for the as-grown films and the samples treated at -50 V for 80 min for both transistor-like and capacitor configurations (Figure 2). Co (red) and O (blue) are homogeneously distributed in the as-grown sample with capacitor configuration (Figure 2d) and nearly homogeneously distributed in the treated sample with the transistor-like configuration (Figure 2e), which sharply contrasts with the sample treated under -50 V in the capacitor configuration (Figure 2f). The corresponding Co (red) and O (blue) EELS mappings reveal the presence of Co-rich and O-rich areas due to voltage-driven ion migration. In contrast to the sample grown on SiO_2 , electrolyte-gating of the Co_3O_4 sample grown on TiN results in bubbling, evidencing that, on top of oxygen redistribution within the film,^[26] oxygen might be also released into the liquid medium, acting as an oxygen sink. Upon negative biases, oxygen ions, negatively charged, effectively move towards the positively charged counter electrode/gate electrode. Upon traversing the liquid electrolyte and reaching the counter electrode, oxygen ions may form O_2 , causing bubbling, which can be visible to the eye.

As can be seen in Figure 2, a thin layer (a few nm in thickness) is present at the TiN/ Co_3O_4 interface, likely caused by interface reaction while growing the Co_3O_4 at 200°C on TiN. By HAADF-STEM, this layer appears darker evidencing its lighter nature compared to the contiguous phases, thus compatible with a TiO_2 -based phase which is the lightest among the possible phases that might form at the TiN/ Co_3O_4 : $\text{TiO}_2 + \text{CoN} + \text{Co}_2\text{N}$, as predicted using the Materials API (MAPI software).^[48]

Further structural characterization was carried out by $\theta/2\theta$ X-ray diffraction (XRD), high resolution transmission electron microscopy (HRTEM) and variable energy positron annihilation spectroscopy (VEPAS). The XRD patterns of the as-prepared samples are consistent with a textured Co_3O_4 phase along (1 1 1), (2 2 2) and (3 1 1) planes. Upon

electrolyte-gating at -50 V for 80 min, the intensity of the (1 1 1) and (2 2 2) planes strongly decreases while that of the (3 1 1) planes reduces only slightly. For the Co_3O_4 sample grown on TiN, the peak corresponding to (1 1 1) planes fully vanishes after the application of this negative voltage (**Figure 3a**). Furthermore, as seen in the detailed XRD view of Figure 3b, the capacitor configuration shows the emergence of a new peak after gating at -200 V for 80 min, which is consistent with the diffraction from (0 0 2) planes of hexagonal close-packed Co (HCP-Co).

Moreover, high resolution transmission electron microscopy (HRTEM) was performed in the cross-section of a Co_3O_4 film grown on TiN and treated at -50 V (Figure 3c). The inset shows the fast Fourier transform of the area marked with a red rectangle, which results in three well-defined spots highlighted in red circles and numbered 1, 2 and 3. The corresponding interplanar distances are 1.991, 1.920 and 2.535 Å, respectively. The interplanar distance of 1.920 Å is unambiguously ascribed to (1 0 1) HCP-Co (ICDD JCPDF 00-005-0727), whereas 1.991 Å could be associated with either (0 0 2) HCP-Co or (4 0 0) Co_3O_4 (ICDD JCPDF 00-009-0418). However, since the as-prepared Co_3O_4 films do not exhibit traces of (4 0 0) planes and (0 0 2) HCP-Co is observed by XRD, the interplanar distance of 1.991 Å is likely to belong to HCP-Co. Finally, 2.535 Å is consistent with an O-deficient (3 1 1) Co_3O_4 (ICDD JCPDF 00-009-0418) phase.^[26]

To examine the microstructure of the as-prepared films at atomic level, variable energy positron annihilation spectroscopy (VEPAS) was performed (Figure 3d). Both low and high electron momentum fraction (S and W , respectively) as a function of positron implantation energy, E_p , virtually overlap up to the first 50 nm in depth. The differences at further depths of the film are essentially due to the different chemical nature of the buffer layer. This indicates that the as-prepared films grown on both substrates have similar amount and type of defects, independently of the substrate they are grown on.

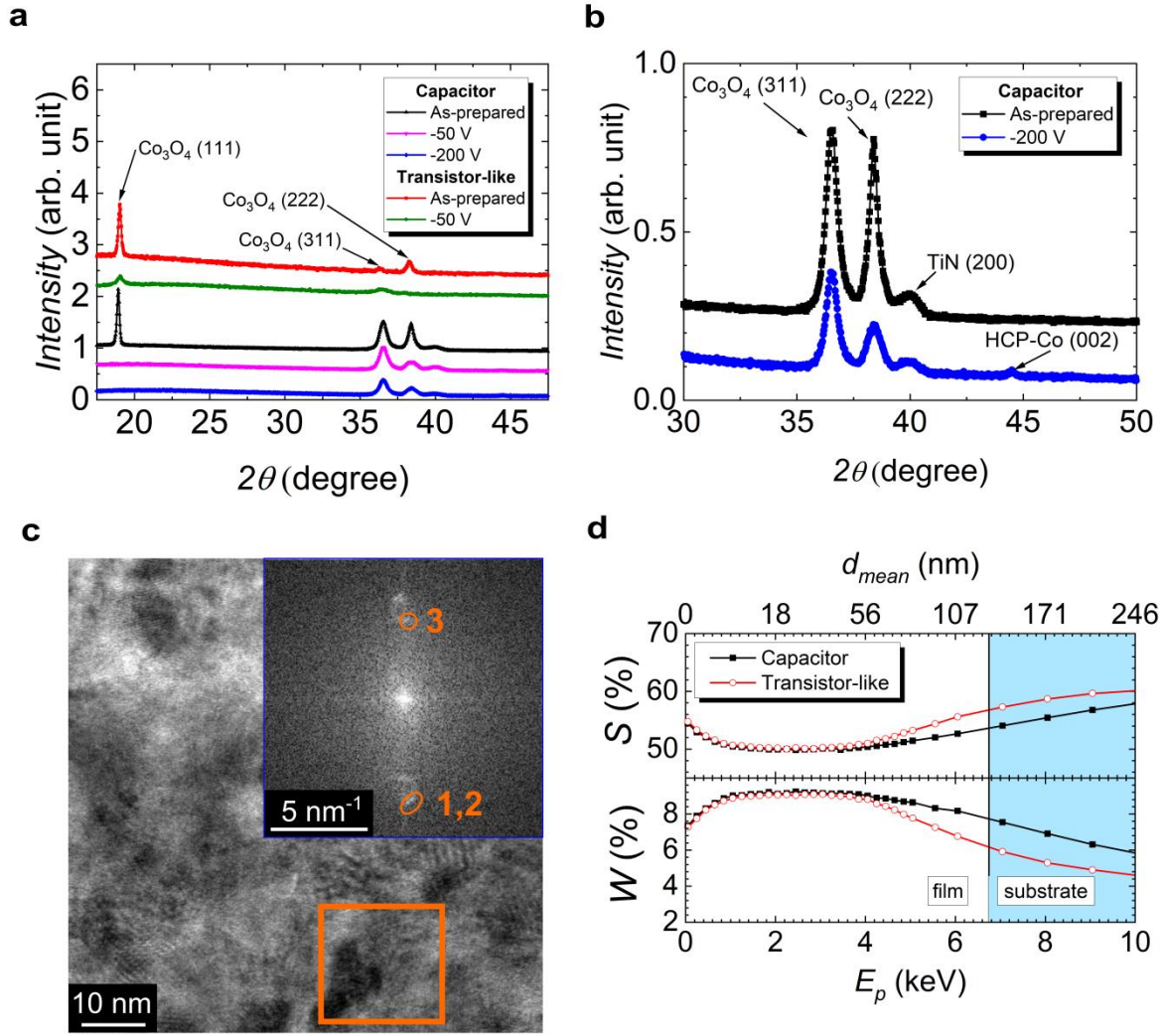


Figure 3. Structural characterization by $\theta/2\theta$ X-ray diffraction (XRD), high resolution transmission electron microscopy (HRTEM) and variable energy positron annihilation spectroscopy (VEPAS). a) $\theta/2\theta$ XRD diffraction patterns of the as-prepared and treated samples at -50 V, and at -200 V for the Co_3O_4 grown on TiN. b) Detailed view of the XRD patterns corresponding to the Co_3O_4 grown on TiN. c) HRTEM image of the cross-section of a Co_3O_4 film grown on TiN and treated at -50 V. The inset shows the fast Fourier transform of the area marked with a red rectangle. d) Low and high electron momentum fraction (S and W , respectively) as a function of positron implantation energy, E_p , for the as-prepared samples. “ d_{mean} ” stands for average depth.

The onset voltage for magneto-ionic motion and cyclability has also been investigated for both configurations (**Figure 4**). To determine the onset voltage, the gating was monotonically decreased in steps of -2 V to observe when the system started to display ferromagnetic behavior. In contrast to the measurements presented in Figure 1 in which consecutive hysteresis loops are acquired while gating the sample, now the film is subjected to a constant applied magnetic field

(specifically, 5 kOe, which is above the anisotropy field of the induced ferromagnetic phase) and the magnetization continuously measured while varying the applied voltage. Afterwards, the voltage polarity was reversed to test the cyclability of the magneto-ionic effect. The Co_3O_4 film grown on TiN exhibits an onset voltage of -4 V and requires of $+50$ V to fully recover the pristine paramagnetic state. Conversely, the transistor-like configuration shows an onset voltage of -10 V and requires of $+10$ V to recover the initial state, in agreement with previously reported results on the same configuration but with a thicker SiO_2 buffer layer.^[26]

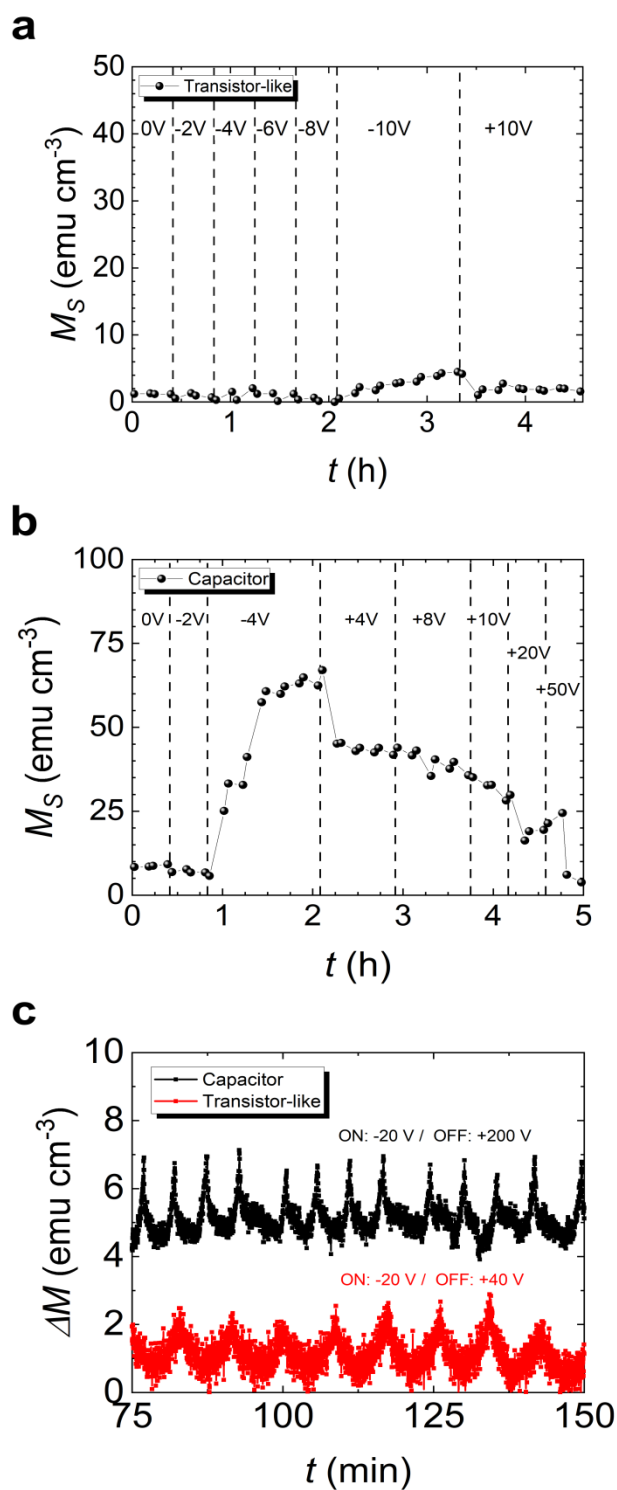


Figure 4. a) and b) onset/recovery behavior of the transistor-like and capacitor configurations, respectively. c) Cyclability for both sample configurations (−20 V/+40 V and −20 V/+200 V pulses for the transistor-like and capacitor configurations, respectively). The data are shifted in ΔM -axis to make them distinguishable among configurations. Cyclability was carried out under the application of 5 kOe to ensure being above the anisotropy field and, thus, in saturation.

While the onset/recovery process is repeatable, to perform cyclability tests the applied biases were increased in order to enhance the magneto-ionic signal-to-noise ratio and, thus, better observe endurance. 30 cycles were performed using voltage pulses of $-20\text{ V}/+40\text{ V}$ and $-20\text{ V}/+200\text{ V}$ for the transistor-like and capacitor configurations, respectively (Figure 4c). The change in magnetization relative to the background magnetization is observed to be repeatable in time scale and magnetization quality, suggesting suitable reproducibility for long term use. The magnetoelectric-voltage coefficient according to reference 26, which is given by $\alpha_{c,v} = \Delta M/|\Delta V|$, has been calculated for both configurations upon inducing magneto-ionics under the conditions of Figure 4c and using an interval of time defined by the base-to-peak time of the cycling of the Co_3O_4 film in capacitor configuration, resulting in coefficients of around 0.01 and $0.11\text{ emu cm}^{-3}\text{ V}^{-1}$ for the Co_3O_4 films in transistor-like and capacitor configurations, respectively.

3. Discussion

The role of the the electric field configuration used during magnetoelectric actuation (electric double layer transistor-like vs. capacitor –condenser-like–) in the magneto-ionic behavior of Co_3O_4 thin films has been investigated. As seen in Figure 1, upon electrolyte-gating at -50 V , the use of an underlying conducting (capacitor) rather than an insulating (transistor-like) buffer layer boosts magneto-ionics in terms of both long-term generated magnetization (6-fold relative increase) and initial magneto-ionic motion (35 times faster).

These different behaviors are already revealed by the M - H hysteresis loops which show pronounced differences in shape. The capacitor configuration results in more square-shaped loops with larger squareness, narrower distribution of coercive fields and higher slopes at H_C , evidencing a more “easy-axis” nature than the transistor-like configuration. This is consistent with the generation of more uniform ferromagnetic regions in the Co_3O_4 film (with better defined shape anisotropy) when a conducting buffer layer is grown, in agreement with the

COMSOL simulations of Figure 1g and 1h. In the transistor-like configuration, the interplay between the dielectric nature of SiO_2 and the limited electric conductivity of Co_3O_4 manifests in a non-homogeneous voltage distribution along the Co_3O_4 film, resulting in a non-uniform electric field which decreases as the distance from the electric contact increases. Conversely, in the capacitor configuration, the conducting nature of TiN results in a nearly uniform electric field along the vertical cross-section of the sample, which gives rise to a larger and better-defined electric field along the direction perpendicular to the Co_3O_4 film plane. In contrast to the transistor-like configuration, the Co_3O_4 film on TiN is fully and homogeneously activated alongside its complete vertical extent. This results in a well-defined path with a nearly full perpendicular electric field component for magneto-ionic motion in the conducting configuration. On the contrary, in the transistor-like configuration, the strength and speed of magneto-ionic motion is hindered due to the limited electric conductivity of Co_3O_4 . This is in concordance with a broader size distribution of ferromagnetic regions in the electrolyte-gated Co_3O_4 film on SiO_2 , in agreement with the magnetometry results which indicate lower squareness values and a broader distribution of coercive fields. This is also evidenced by the evolution of coercivity with time for the consecutive loops taken while electrolyte-gating both configurations at -50 V (Figure S6). Whereas the transistor-like configuration results in a monotonic increase of H_C with time, the electrochemical capacitor configuration shows a maximum at the very beginning. This maximal behavior resembles the typical dependence of coercivity with particle size in magnetic systems, consistent with a scenario in which a more homogeneous generation of ferromagnetic regions occurs, uniformly evolving in size, likely starting from a superparamagnetic behavior, followed by a single domain state (maximum of H_C) and ending with a multi-domain state.^[46]

The effect of electric field configuration on the compositional and structural properties of Co_3O_4 is clearly observed in Figure 2. The morphology of the pristine samples shows regular, columnar-shaped grains (Figure 2a and Figure S5) and homogeneous composition (Figure 2d).

This largely remains upon treating the Co_3O_4 film deposited on SiO_2 with -50 V for 80 min (Figure 2b and 2e). Conversely, the morphology of the film in the capacitor configuration treated at -50 V for 80 min shows almost no columnar grains and a highly nanostructured Co_3O_4 phase (Figure 2c and Figure S5) with Co and O segregation (Figure 2f). This indicates that this configuration can electrically modulate ion migration at much higher strengths. This is further confirmed by XRD and HRTEM which show traces of metallic Co only for the capacitor configuration (Figure 3). Even though the as-prepared Co_3O_4 films show similar crystallographic features regardless of the buffer layer, further structural characterization to examine the local microstructure of the as-prepared samples was carried out by VEPAS. As seen in Figure 3d, both low and high electron momentum fraction (S and W , respectively) as a function of positron implantation energy, E_p , virtually overlap, indicating that Co_3O_4 grown on either SiO_2 or TiN exhibits analogous defect environment, ruling out minor microstructure differences in Co_3O_4 as the origin of the observed magneto-ionic effects. Nevertheless, the crystalline orientation seem to play a role in the voltage-driven ion diffusion, which is facilitated along (1 1 1) planes as evidenced by the strong decrease in intensity of the (1 1 1) and (2 2 2) planes, with the (1 1 1) planes fully vanishing for the Co_3O_4 sample grown on TiN (Figure 3a). As seen in Figure 4, the minimum voltage bias required to perform an onset/recovery cycle is asymmetric for the Co_3O_4 film grown on TiN (-4 V/ $+50$ V), while it is symmetric for the Co_3O_4 film grown on SiO_2 (-10 V/ $+10$ V). The onset bias is significantly larger for the transistor-like configuration (-4 V (conducting TiN) vs. -10 V (insulating SiO_2)). In contrast to the transistor-like configuration, the use of a conducting buffer layer activates the whole Co_3O_4 sample, resulting in a more intense and better defined perpendicular electric field and, thus, in enhanced magneto-ionic effect and motion. Bubbling is noticeably observable only in the electrochemical capacitor configuration, evidencing that, on top of oxygen redistribution,^[26] oxygen may be released into the liquid electrolyte, which might act as an oxygen sink, and as an oxygen reservoir due to the oxygen solubility in propylene carbonate.^[47] The voltage asymmetry in the

capacitor configuration can be linked to O₂ bubbling since propylene carbonate reaches O supersaturation and the oxygen forming bubbles cannot be recovered. Moreover, partial degradation of propylene carbonate cannot be ruled out as an additional origin of bubbling since it may result among others in propylene gas.^[49]

Cycling (Figure 4) further corroborates the faster magneto-ionic rates of the electrochemical capacitor configuration, particularly during the generation of the “on” states. Time span in the transistor-like configuration has been enlarged to reach a suitable signal-to-noise ratio, as a consequence of the slower magneto-ionic kinetics. For the capacitor configuration, cyclability is lost when lower voltages (higher in absolute value but negatively biased) are applied (*e.g.*, –50 V) due to strong irreversible bubbling.

4. Conclusion

The role of the electric field configuration (determined by the electrical properties of the substrate/buffer layer) in the magneto-ionic behavior of Co₃O₄ thin films has been investigated. Polycrystalline 130 nm-thick Co₃O₄ films have been grown by atomic layer deposition on either insulating SiO₂ or conducting TiN buffer layers. The use of an electrochemical capacitor configuration rather than contacting the semiconducting layer using a transistor-like configuration boosts magneto-ionics in terms of both generated magnetization (6-fold increase: from 118.5 (Co₃O₄/SiO₂) to 699.2 emu cm⁻³ (Co₃O₄/TiN)) and magneto-ionic rates (35 times faster: from 33.1 (Co₃O₄/SiO₂) to 1170.8 emu cm⁻³ h⁻¹ (Co₃O₄/TiN)). The magneto-ionic rate for the capacitor configuration is of the same order of magnitude ($\sim 10^3$ emu cm⁻³ h⁻¹) than that one achieved in other systems using magnetization as a figure of merit to track magneto-ionic effects, such as Li-ion intercalation-based magneto-ionics.^[35] Even though the voltage required is larger for our system, our results are promising in terms of speed since our work deals with both relatively thick films (rather than nanoparticles which exhibit a much higher surface-to-volume ratio) and oxygen ions (larger than Li ions). In our system, the magneto-ionic speed

could be strongly increased by system miniaturization and/or a local modulation of properties, such as magnetic domains.^[50] Upon gating, transmission electron microscopy and electron energy loss spectroscopy show the emergence of Co-rich areas at a greater intensity for the Co_3O_4 grown on an electrically conducting substrate. Magnetization measurements also show a marked increase in the squareness ratio and a decrease in the switching field distribution of the hysteresis loops from Co_3O_4 deposited in the capacitor configuration, evidencing the generation of more uniform ferromagnetic regions. This dissimilar behavior between the use of either an insulating or a conducting substrate arises from the intensity and uniformity of the electric field, which are maximized when using a conducting substrate while preserving stability and endurance. These results demonstrate the importance of the specific device design in order to optimize the strength and speed of the magneto-ionic effect. Our results prompt the way to make oxygen magneto-ionics feasible for practical applications in fields like neuromorphic and stochastic computing or magnetic MEMS, where high frequencies are not necessarily required for device engineering.^[39]

5. Experimental Section

Sample preparation: 130 nm thick Co_3O_4 films were grown on two substrates: i) thermally oxidized non-doped Si wafers (SiO_2 (20 nm)/(1 0 0)-oriented Si (0.5 mm)), and ii) non-doped Si wafers coated with a TiN buffer layer (TiN (170 nm)/(1 0 0)-oriented Si (0.5 mm)). The deposition of Co_3O_4 was carried out by plasma enhanced atomic layer deposition as described in references 26, 51 and 52. The TiN buffer layer was grown by reactive sputtering using the conditions reported in reference 37. TiN was selected because of its conductivity and thermal stability allows proper growth of the Co_3O_4 film which is carried out at 200 °C by plasma enhanced atomic layer deposition.

Magnetoelectric characterization: Magnetic measurements under electrolyte gating (*i.e.*, magnetoelectric characterization) were carried out at room-temperature in a vibrating sample magnetometer from Micro Sense (LOT-Quantum Design), with a maximum applied magnetic field of 2 T. Two different configurations were implemented, an electrochemical capacitor one and an electric double layer transistor-like design, where electric contacts are just made on top and at the sides of the semiconducting layer. The sample was mounted in a homemade electrolytic cell filled with anhydrous propylene carbonate with Na⁺ solvated species (5 - 25 ppm), and the magnetic properties were measured along the film plane after applying different voltages, using an external Agilent B2902A power supply, between the sample and the counter-electrode in a similar fashion of that presented in references 16, 26 and 34. The Na⁺ solvated species in the electrolyte are aimed at reacting with any traces of water.^[16] The magnetic signal was normalized to the area of the sample exposed to the electrolyte during the voltage application process. All hysteresis loops were background-corrected and the correction was carried out at high fields (*i.e.*, fields always far above saturation fields) to eliminate linear contributions (paramagnetic and diamagnetic signals).

Structural and compositional measurements: $\theta/2\theta$ X-ray diffraction (XRD) patterns were recorded on a Philips X'Pert Powder diffractometer with a PIXcel^{1D} detector using Cu K α radiation.

High resolution transmission electron microscopy (HRTEM), high-angle annular dark-field scanning transmission electron microscopy (HAADF-STEM) and electron energy loss spectroscopy (EELS) were performed on a TECNAI F20 HRTEM /STEM microscope operated at 200 kV. Cross sectional lamellae were prepared by focused ion beam and placed onto a Cu transmission electron microscopy grid.

Variable energy positron annihilation spectroscopy (VEPAS)^[53,54] was used to investigate depth-resolved open volume defects at the Slow-Positron System of Rossendorf (SPONSOR) beamline, which provides monoenergetic but variable energy positron beam.

Modelling: A simulation of the charge distribution in each of the two systems was performed using COMSOL finite element analysis software. Estimation of the charge distribution considered charge conservation ($\nabla J = 0$), Ohm's law ($J = \sigma E$), and Gauss' law ($E = -\nabla V$). The geometry of the system was modeled in 2D to minimize computation needs. The geometry includes the silicon substrate (0.5 mm), the sample film (Co_3O_4 and buffer layer: either SiO_2 or TiN), contact layer (In solder onto Cu wire), a platinum counter electrode, all set in an electrochemical chamber filled with propylene carbonate. The sample film has been unified to enable a tetragonal adaptive mesh within the computer memory resources. The effective electric conductivity (*i.e.*, electric conductance) has been modeled by weighing the different sub-layer constituting within the sample stack and normalizing relative to the thicknesses of each layer in the model. In the transistor-like configuration the silicon substrate is considered coated with a SiO_2 layer, electrically isolated from the sample. The sample essentially consists of a 130 nm Co_3O_4 layer on top the substrate. A value of electrical conductivity of 20 S/m for Co_3O_4 has been measured via a 4-probe van der Pauw measurement, in agreement with values from the literature.^[51]

The electrical conductivity for TiN was taken from literature, 3.3×10^5 S/m.^[45] In the capacitor configuration, the 170 nm of TiN and the 130 nm of Co_3O_4 are taken in combination. The large electrical conductivity of the TiN dominates the effective electrical conductivity of the sample section. Simulations shown are calculated for the system under -50 V gating voltage. The propylene carbonate has been modeled as an insulator with a conductivity of 4.6×10^{-4} S/m and a relative dielectric permittivity of 65^[55] with the aim to properly model the charge densities and the voltage at the surface of the Co_3O_4 film.

Supporting Information

Supporting Information is available from the Wiley Online Library or from the author.

Acknowledgements

Financial support by the European Research Council (SPIN-PORICS 2014-Consolidator Grant, Agreement N° 648454), the Spanish Government (MAT2017-86357-C3-1-R), the Generalitat de Catalunya (2017-SGR-292 and 2018-LLAV-00032) and the European Regional Development Fund (MAT2017-86357-C3-1-R and 2018-LLAV-00032) is acknowledged. This work was partially supported by the Impulse-und Net-working fund of the Helmholtz Association (FKZ VH-VI-442 Memriox), and the Helmholtz Energy Materials Characterization Platform (03ET7015). The PALS measurements were carried out at ELBE at the Helmholtz-Zentrum Dresden-Rossendorf e. V., a member of the Helmholtz Association. The authors would like to thank Ahmed G. Attallah and Eric Hirschmann for assistance during the VEPAS measurements.

Received: ((will be filled in by the editorial staff))

Revised: ((will be filled in by the editorial staff))

Published online: ((will be filled in by the editorial staff))

References

- [1] D. A. Patterson, J. L. Hennessy, *Computer Organization and Design: The Hardware/Software Interface*, 5th edition, Elsevier Inc., Amsterdam **2014**.
- [2] H. An, K. Bai, Y. Yi, *Advances in Memristor Neural Networks - Modeling and Applications* (Ed: C. Ciufudean), IntechOpen, **2018**, 25–44 (The roadmap to realize memristive three-dimensional neuromorphic computing system).
- [3] Q. Xia, J. J. Yang, *Nat. Mater.* **2019**, *18*, 309.
- [4] J. Torrejon, M. Riou, F. A. Araujo, S. Tsunegi, G. Khalsa, D. Querlioz, P. Bortolotti, V. Cros, K. Yakushiji, A. Fukushima, H. Kubota, S. Yuasa, M. D. Stiles, J. Grollier, *Nature* **2017**, *547*, 428.
- [5] S. Manipatruni, D. E. Nikonov, I. A. Young, *Nat. Phys.* **2018**, *14*, 338.
- [6] R. Mishra, D. Kumar, H. Yang, *Phys. Rev. Appl.* **2019**, *11*, 054065.

- [7] Y. Shiota, T. Nozaki, F. Bonell, S. Murakami, T. Shinjo, Y. Suzuki, *Nat. Mater.* **2012**, *11*, 39.
- [8] C. Song, B. Cui, F. Li, X. Zhou, F. Pan, *Prog. Mater. Sci.* **2017**, *87*, 33.
- [9] M. Bibes, A. Barthélémy, *Nat. Mater.* **2008**, *7*, 425.
- [10] S. Marauska, R. Jahns, H. Greve, E. Quandt, R. Knöchel, B. Wagner, *J. Micromech. Microeng.* **2012**, *22*, 065024.
- [11] W. Eerenstein, N. D. Mathur, J. F. Scott, *Nature* **2006**, *442*, 759.
- [12] Y. Wang, J. Hu, Y. Lin, C.-W. Nan, *NPG Asia Mater.* **2010**, *2*, 61.
- [13] P. Li, Y. Zhao, S. Zhang, A. Chen, D. Li, J. Ma, Y. Liu, D. T. Pierce, J. Unguris, H.-G. Piao, H. Zhang, M. Zhu, X. Zhang, X. Han, M. Pan, C.-W. Nan, *ACS Appl. Mater. Interfaces* **2017**, *9*, 2642.
- [14] M. Weisheit, S. Fähler, A. Marty, Y. Souche, C. Poinsignon, D. Givord, *Science* **2007**, *315*, 349.
- [15] M. Zhernenkov, M. R. Fitzsimmons, J. Chlistunoff, J. Majewski, I. Tusoda, E. E. Fullerton, *Phys. Rev. B* **2010**, *82*, 024420.
- [16] A. Quintana, J. Zhang, E. Isarain-Chávez, E. Menéndez, R. Cuadrado, R. Robles, M. D. Baró, M. Guerrero, S. Pané, B. J. Nelson, C. M. Müller, P. Ordejón, J. Nogués, E. Pellicer, J. Sort, *Adv. Funct. Mater.* **2017**, *27*, 1701904.
- [17] A. K. Mishra, C. Bansal, M. Ghafari, R. Kruk, H. Hahn, *Phys. Rev. B* **2010**, *81*, 155452.
- [18] S. Ghosh, *J. Magn. Magn. Mater.* **2011**, *323*, 552.
- [19] S. Ghosh, C. Lemier, J. Weissmüller, *IEEE Trans. Magn.* **2006**, *42*, 3617.
- [20] A. K. Mishra, A. J. Darbandi, P. M. Leufke, R. Kruk, H. Hahn, *J. Appl. Phys.* **2013**, *113*, 033913.

- [21] K. Duschek, M. Uhlemann, H. Schlörb, K. Nielsch, K. Leistner, *Electrochem. Commun.* **2016**, *72*, 153.
- [22] U. Bauer, L. Yao, A. J. Tan, P. Agrawal, S. Emori, H. L. Tuller, S. van Dijken, G. S. D. Beach, *Nat. Mater.* **2015**, *14*, 174.
- [23] D. A. Gilbert, A. J. Grutter, E. Arenholz, K. Liu, B. J. Kirby, J. A. Borchers, B. B. Maranville, *Nat. Commun.* **2016**, *7*, 12264.
- [24] D. A. Gilbert, J. Olamit, R. K. Dumas, B. J. Kirby, A. J. Grutter, B. B. Maranville, E. Arenholz, J. A. Borchers, K. Liu, *Nat. Commun.* **2016**, *7*, 11050.
- [25] L. Baldrati, A. J. Tan, M. Mann, R. Bertacco, G. S. D. Beach, *Appl. Phys. Lett.* **2017**, *110*, 012404.
- [26] A. Quintana, E. Menéndez, M. O. Liedke, M. Butterling, A. Wagner, V. Sireus, P. Torruella, S. Estradé, F. Peiró, J. Dendooven, C. Detavernier, P. D. Murray, D. A. Gilbert, K. Liu, E. Pellicer, J. Nogues, J. Sort, *ACS Nano* **2018**, *12*, 10291.
- [27] C. Navarro-Senent, J. Fornell, E. Isarain-Chávez, A. Quintana, E. Menéndez, M. Foerster, L. Aballe, E. Weschke, J. Nogués, E. Pellicer, J. Sort, *ACS Appl. Mater. Interfaces* **2018**, *10*, 44897.
- [28] F. Ibrahim, A. Hallal, B. Dieny, M. Chshiev, *Phys. Rev. B* **2018**, *98*, 214441.
- [29] A. J. Tan, M. Huang, C. O. Avci, F. Büttner, M. Mann, W. Hu, C. Mazzoli, S. Wilkins, H. L. Tuller, G. S. D. Beach, *Nat. Mater.* **2019**, *18*, 35.
- [30] A. J. Tan, M. Huang, S. Sheffels, F. Büttner, S. Kim, A. H. Hunt, I. Waluyo, H. L. Tuller, G. S. D. Beach, *Phys. Rev. Mater.* **2019**, *3*, 064408.
- [31] A. Molinari, H. Hahn, R. Kruk, *Adv. Mater.* **2019**, *31*, 1806662.
- [32] S. Robbennolt, A. Nicolenco, P. M. Fernandez, S. Auffret, V. Batz, E. Pellicer, E. Menéndez, J. Sort, *ACS Appl. Mater. Interfaces* **2019**, *11*, 37338.

- [33] S. Robbennolt, E. Menéndez, A. Quintana, A. Gómez, S. Auffret, V. Batz, E. Pellicer, J. Sort, *Sci. Rep.* **2019**, *9*, 10804.
- [34] C. Navarro-Senent, A. Quintana, E. Menéndez, E. Pellicer, J. Sort, *APL Mater.* **2019**, *7*, 030701.
- [35] S. Dasgupta, B. Das, M. Knapp, R. A. Brand, H. Ehrenberg, R. Kruk, H. Hahn, *Adv. Mater.* **2014**, *26*, 4639.
- [36] S. Dasgupta, B. Das, Q. Li, D. Wang, T. T. Baby, S. Indris, M. Knapp, H. Ehrenberg, K. Fink, R. Kruk, H. Hahn, *Adv. Funct. Mater.* **2016**, *26*, 7507.
- [37] S. Vasala, A. Jakob, K. Wissel, A. I. Waidha, L. Alff, O. Clemens, *Adv. Electron. Mater.* **2020**, *6*, 1900974.
- [38] T. Fujimoto, K. Awaga, *Phys. Chem. Chem. Phys.* **2013**, *15*, 8983.
- [39] C. Leighton, *Nat. Mater.* **2019**, *18*, 13.
- [40] Y. Yamada, K. Ueno, T. Fukumura, H. T. Yuan, H. Shimotani, Y. Iwasa, L. Gu, S. Tsukimoto, Y. Ikuhara, M. Kawasaki, *Science* **2011**, *332*, 1065.
- [41] J. Walter, T. Charlton, H. Ambaye, M. R. Fitzsimmons, P. P. Orth, R. M. Fernandes, C. Leighton, *Phys. Rev. Mater.* **2018**, *2*, 111406(R).
- [42] J. G. Checkelsky, J. Ye, Y. Onose, Y. Iwasa, Y. Tokura, *Nat. Phys.* **8**, 729–733 (2012).
- [43] S. Z. Bisri, S. Shimizu, M. Nakano, Y. Iwasa, *Adv. Mater.* **2017**, *29*, 1607054.
- [44] J. J. Harris, R. Jolivet, D. Attwell, *Neuron* **2012**, *75*, 762.
- [45] K. Kawabata, T. Muto, *Electrocomp. Sci. Technol.* **1981**, *8*, 249.
- [46] D. L. Leslie-Pelecky, R. D. Rieke, *Chem. Mater.* **1996**, *8*, 1770.
- [47] W. R. Baird, R. T. Foley, *J. Chem. Eng. Data* **1972**, *17*, 355.
- [48] <https://materialsproject.org/open>, accessed: November, 2019.

- [49] G. Eichinger, *J. Electroanal. Chem. Interfacial Electrochem.* **1976**, 74, 183.
- [50] X. Zhu, J. Zhou, L. Chen, S. Guo, G. Liu, R.-W. Li, W. D. Lu, *Adv. Mater.* **2016**, 28, 7658.
- [51] M. E. Donders, H. C. M. Knoops, M. C. M. van de Sanden, W. M. M. Kessels, P. H. L. Notten, *J. Electrochem. Soc.* **2011**, 158, G92.
- [52] J. Dendooven, D. Deduytsche, J. Musschoot, R. L. Vanmeirhaeghe, C. Detavernier, *J. Electrochem. Soc.* **2010**, 157, G111–G116.
- [53] W. Anwand, G. Brauer, M. Butterling, H. R. Kissener, A. Wagner, *Defect Diffus. Forum.* **2012**, 331, 25.
- [54] R. Krause-Rehberg, H. Leipner, *Positron Annihilation in Semiconductors*, Springer, Berlin **1999**.
- [55] S. Xiao, J. F. Kolb, M. A. Malik, X. Lu, M. Laroussi, R. P. Joshi, E. Schamiloglu, K. H. Schoenbach, *IEEE Trans. Plasma Sci.* **2006**, 34, 1653.

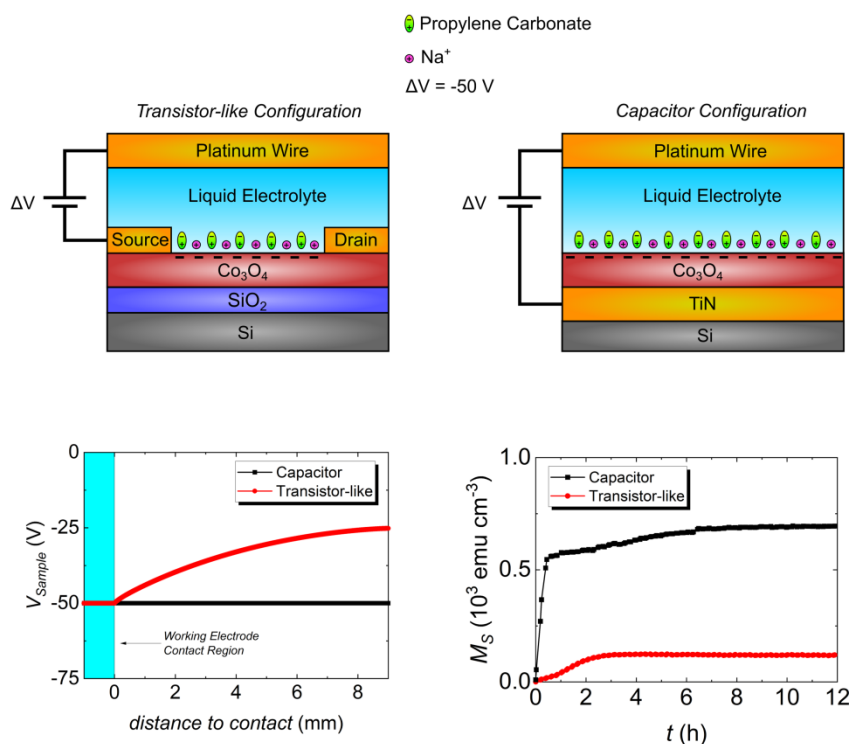
Electric field-induced oxygen motion (magneto-ionics) could represent a significant breakthrough in low-power magnetically-actuated devices. By applying the electric field using an electrochemical capacitor instead of a transistor-like configuration, room-temperature magneto-ionic effects in electrolyte-gated paramagnetic Co_3O_4 films can be largely increased in terms of generated magnetization and speed. This might widen the use of magneto-ionics in technological applications such as neuromorphic computing or iontronics.

Magneto-ionics

Julius de Rojas, Alberto Quintana, Aitor Lopeandía, Joaquín Salguero, José L. Costa-Krämer, Llibertat Abad, Maciej O. Liedke, Maik Butterling, Andreas Wagner, Lowie Henderick, Jolien Dendooven, Christophe Detavernier, Jordi Sort*, Enric Menéndez*

Boosting room-temperature magneto-ionics in a non-magnetic oxide semiconductor

ToC figure



Copyright WILEY-VCH Verlag GmbH & Co. KGaA, 69469 Weinheim, Germany, 2018.

Supporting Information

Boosting room-temperature magneto-ionics in a non-magnetic oxide semiconductor

Julius de Rojas, Alberto Quintana, Aitor Lopeandía, Joaquín Salguero, José L. Costa-Krämer, Llibertat Abad, Maciej O. Liedke, Maik Butterling, Andreas Wagner, Lowie Henderick, Jolien Dendooven, Christophe Detavernier, Jordi Sort*, Enric Menéndez*

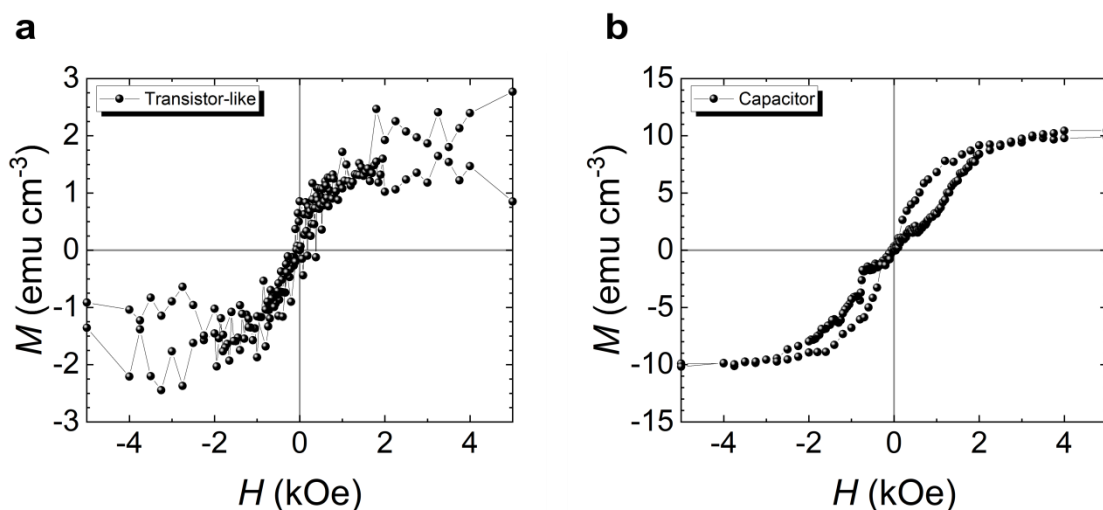


Figure S1. a) and b) are the hysteresis loops of as-prepared Co_3O_4 films grown on SiO_2 (transistor-like configuration) and TiN (capacitor configuration), respectively, taken by in-plane vibrating sample magnetometry.

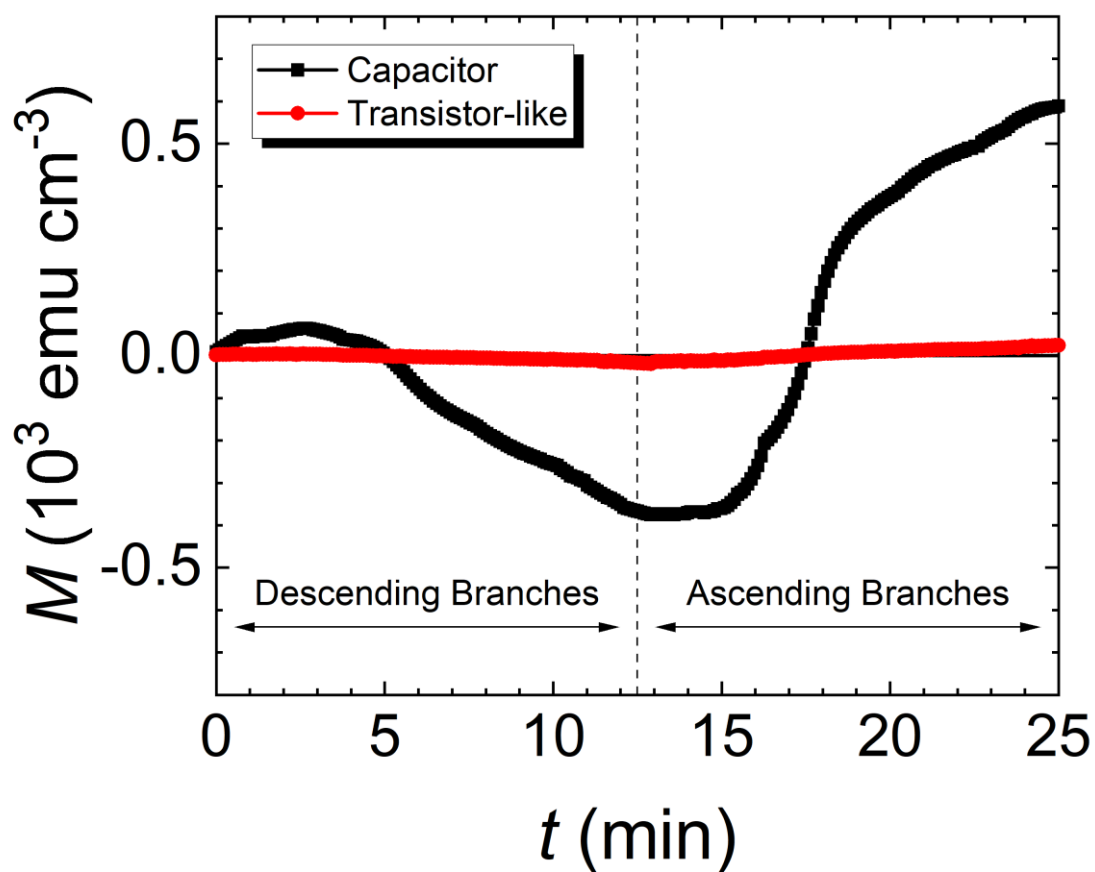


Figure S2. Time evolution of the magnetization (M) for the first hysteresis loop taken upon gating at -50 V for both capacitor (TiN) and transistor-like (SiO_2) configurations.

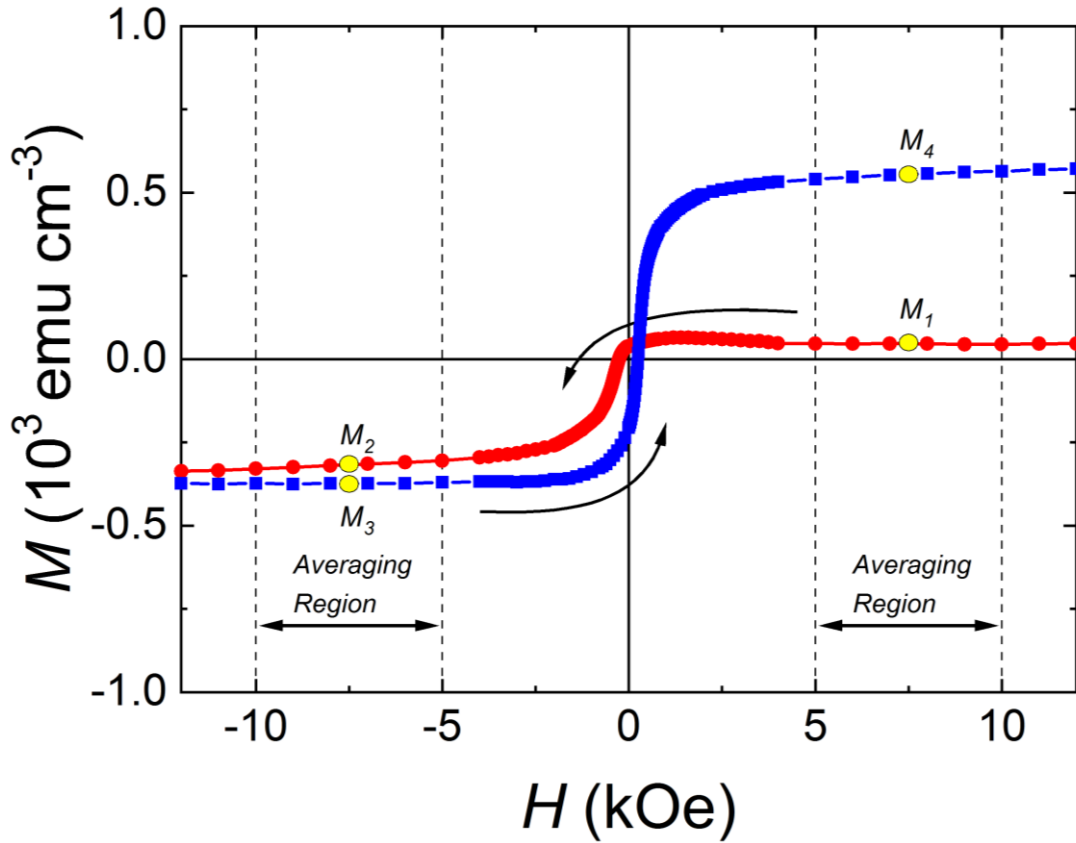


Figure S3. Saturation magnetization (M_S) from evolving hysteresis loops. The cartoon is based on the first hysteresis loop of the Co_3O_4 film grown on TiN (capacitor configuration) upon electrolyte-gating at -50 V. The loops are first slope-corrected for linear background contributions. For each branch (*i.e.*, descending and ascending) of the loop, M_S is calculated in the negative and positive field regions above the anisotropy field: between 5 and 10 kOe in the positive field range, and -10 and -5 kOe in the negative field range (highlighted with arrows). An average of the points is found as the effective M_S (indicated with yellow dots): M_1 , M_2 , M_3 and M_4 , and associated with a time during the measurement of the loop. The time involved in this averaging region is half a minute.

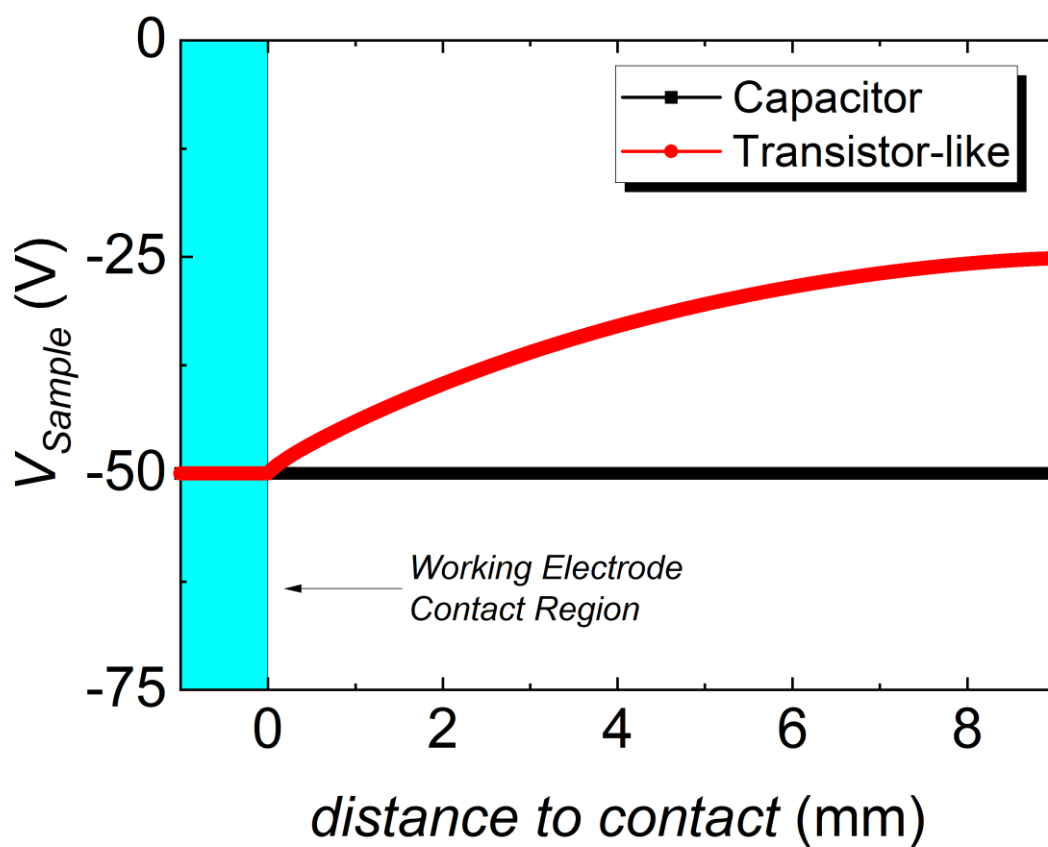


Figure S4. Voltage distribution (upon electrolyte-gating at -50 V) at the surface of the Co_3O_4 layer along the length of the sample for both configurations: Co_3O_4 on either SiO_2 (transistor-like configuration) or TiN (capacitor).

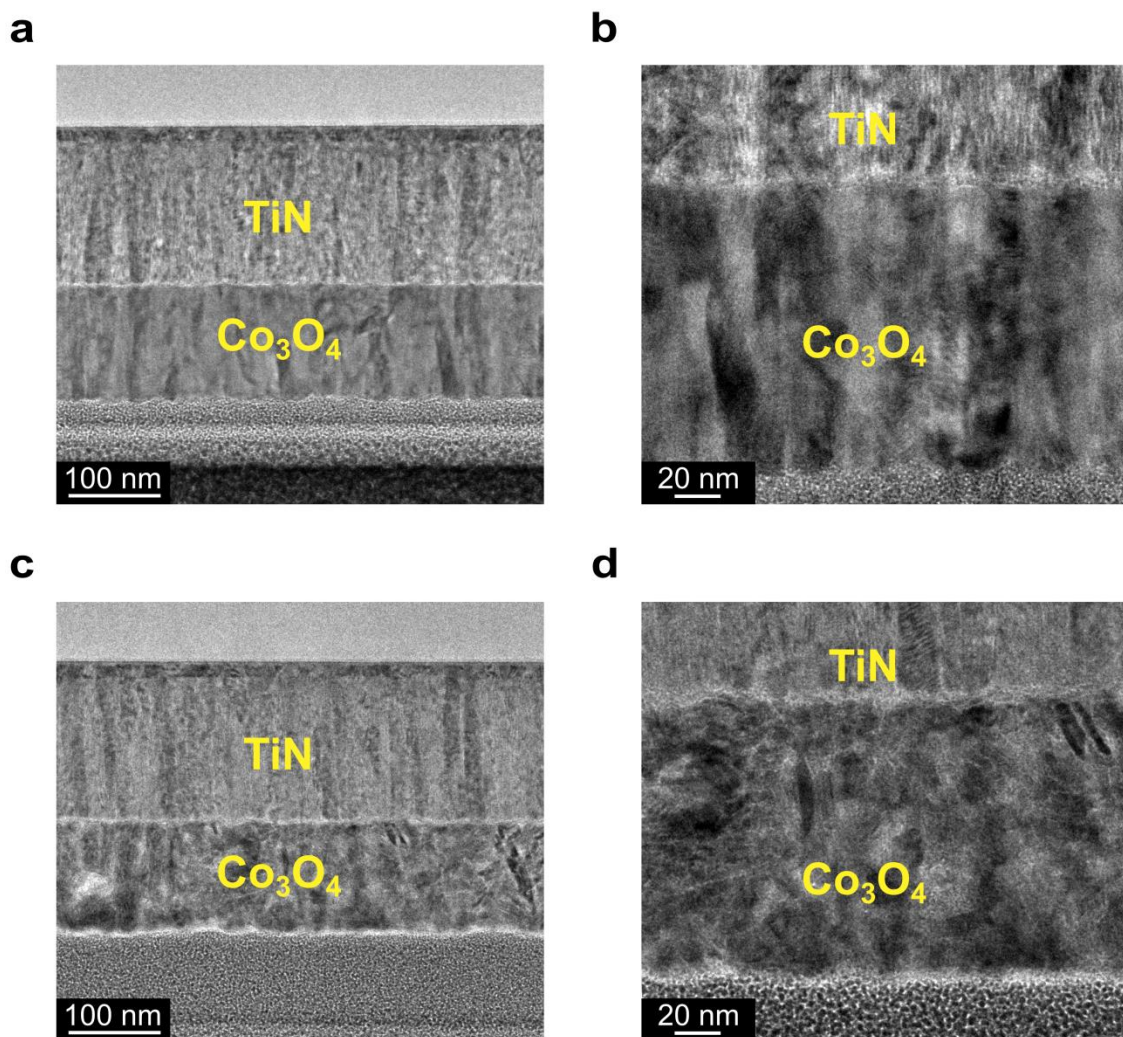


Figure S5. a) and b) are transmission electron microscopy (TEM) images of the cross-section of an as-prepared Co₃O₄ film grown on TiN, and c) and d) are TEM images corresponding to the same sample but treated at -50 V for 80 min.

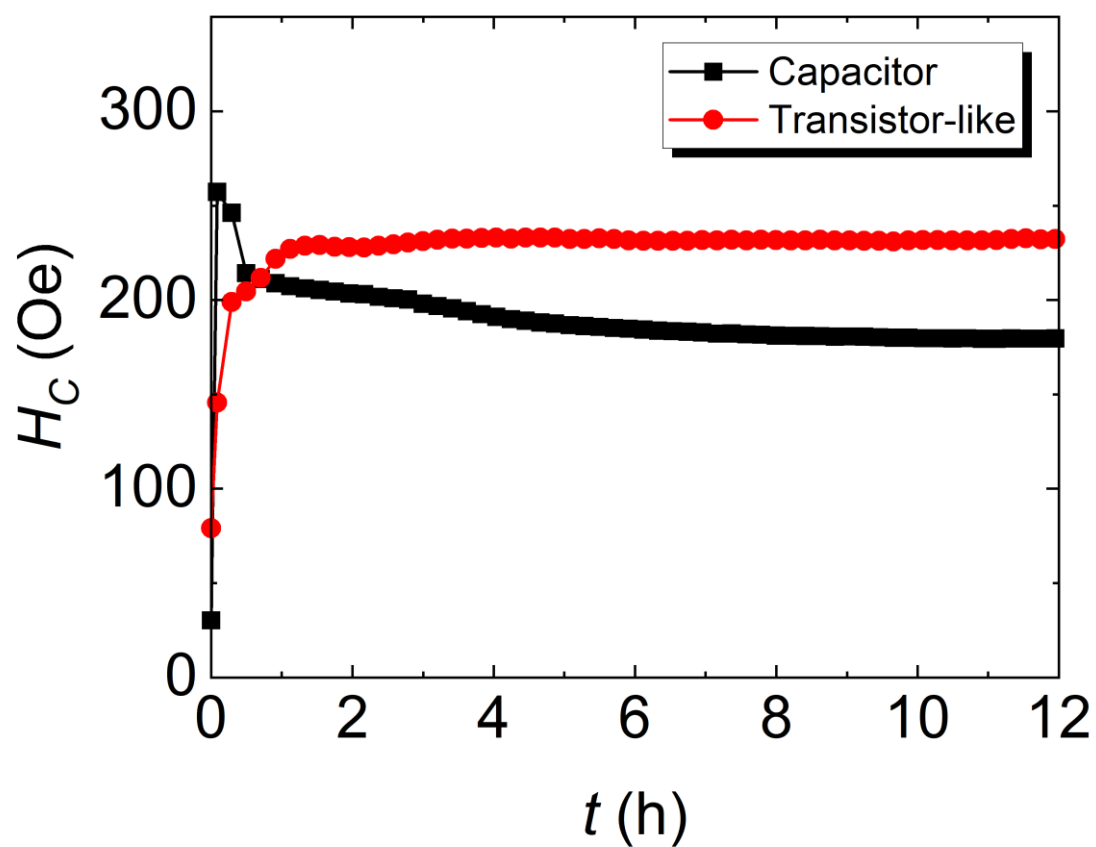


Figure S6. Coercive field (H_C) evolution with time for Co_3O_4 films grown on either SiO_2 (transistor-like configuration) or TiN (capacitor) subjected to a voltage of -50 V for several hours.